Supporting Information

The Acupuncture Effect of Carbon Nanotubes Induced by the Volume Expansion of Silicon-Based Anodes

Ziying He, Chenxi Zhang, Yukang Zhu, Fei Wei*

[1]Beijing Key Laboratory of Green Chemical Reaction Engineering and Technology, Department of Chemical Engineering, Tsinghua University, Beijing 100084, People's Republic of China.

* Corresponding authors. Tel: 010-62785464. E-mail: wf-dce@tsinghua.edu.cn (Fei Wei)

Experimental Section

Preparation of SiO_x@C.

The commercial SiO_x powder (Flotu, ≈3 μm) was added to a glucose solution with a 60% solid content and vigorously stirred for 1 h. Then, the suspension solution underwent a spraying drying process to obtain secondary particles, which were introduced into a Φ50 fluidized bed reactor. When the temperature reached 800 °C under an Ar atmosphere, the carbon source (CH_4) was introduced at a ratio of 1:2 (CH_4 : Ar), in a total flux of 500h^{-1}. Then, the system temperature was held for 45 min until the CVD carbon coating reaction was completed. After the system was cooled naturally to room temperature, the solid product was collected.

Fabrication of electrodes.

Carbon nanotubes were grown using a floating-catalyst CVD technique with methane (CH_4) as the carbon source, and catalyst particles were produced by decomposition of ferrocene vapor ($FeCp_2$, 99%). The CNT networks were collected at room temperature and combined with active materials (SiO_x@C). Finally, press the integration under the roller press.

Fabrication of SW-l LiF-rich electrodes and MW-l LiF-rich electrodes

To prepare LiF-rich electrodes, bare electrodes were firstly soaked into the $LiPF_6$ aqueous solution with 1wt.% H_2O for 12 h. Then it was washed by deionized water for three times, respectively. All materials are kept in the glove box with oxygen and water contents below 5 ppm.

Materials Characterization.

Surface morphology of the electrodes was observed under the field emission scanning electron microscopy (FESEM, JSM 7401, JEOL Co. Ltd., Japan) at an operating voltage of 1.5 kV.

The chemical bonding of the elements in cycled electrodes were verified through X-ray photoelectron spectroscopy (XPS, Thermo Fisher, ESCALAB 250Xi) equipped with Al-Kα (hν=1486.6 eV) radiation with 100 eV.

The Time-of-flight secondary-ion mass spectroscopy (ULVAC-PHI, Japan) was applied to observe the distribution of secondary ions on the electrode surface.

In situ Raman spectroscopy during galvanostatic cycling was performed in a Raman Flow Cell 031–2H to characterize the electrodes during cycling in 1 M $LiPF_6$ with EC, DEC, and DMC (volume ratio = 2:1:2) with 10 wt.% FEC as the electrolyte. The cell

was assembled in an argon filled glovebox (H_2O and O_2 content < 1 ppm) as described in previous studies. The confocal Raman microscope (HR Evolution) with a 532 nm wavelength laser focused through a microscope (Olympus), via 50× long work distance objective (Olympus). Filters were used to reduce the laser power applied on the electrode surface to less 1% (ca. 0.3 mW) for in situ characterization. A baseline correction was applied to all the spectra for clarity, unless otherwise stated. Electrochemical measurements were performed using a CHI 760E electrochemical workstation. An original Raman spectrum was collected before cycling. After power on, collect the spectrum every 0.1 V.

Electrochemical measurements.

The electrochemical measurements were performed using CR2032-type coin cells assembled in an Ar-filled glovebox (with O_2 < 0.1 ppm and H_2O < 0.1 ppm). For the assembly of half-cells, several components were employed: Celgard 2500 film as the separator, lithium foil as the counter electrode, and 1 m LiPF6 as solute in a cosolvent of EC, DEC, and DMC (volume ratio = 2:1:2) with 10 wt.% FEC as the electrolyte.

Galvanostatic cycle measurements were conducted on a LAND-CT2001A battery tester or a Neware CT-4000 battery tester with the voltage window 0.01-1.5. EIS measurements were performed on a BioLogic Science Instruments VSP-300 electrochemical workstation in the frequency range from 1 MHz to 0.01 Hz at the temperature of 25, 35, 45 °C.

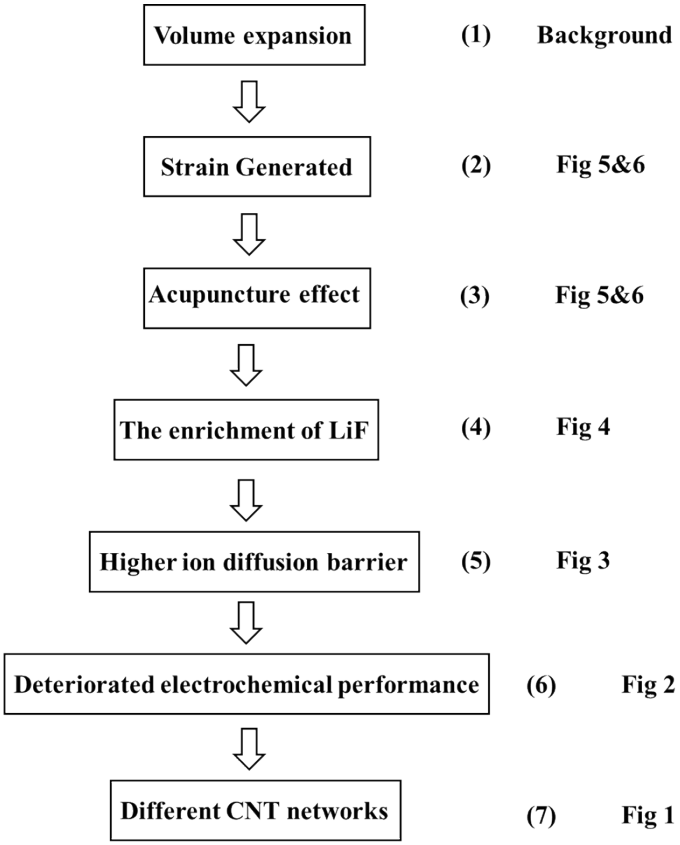

Fig.S1 The logic of this work.

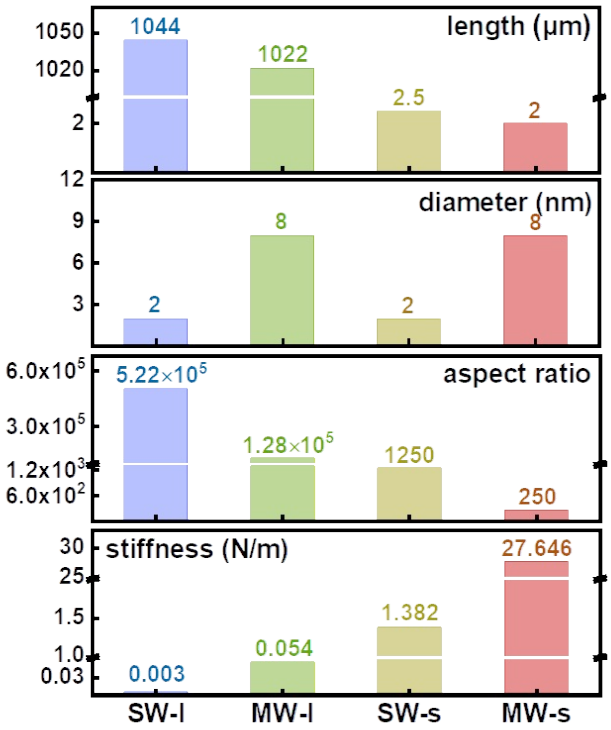

Fig. S2 The average length, diameter, aspect ratio and stiffness of different CNTs.

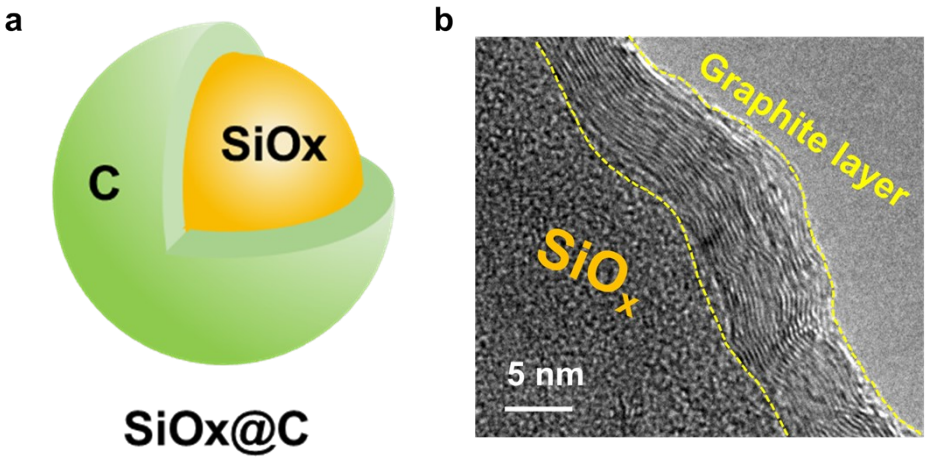

Fig. S3 The structure of SiOx@C.
(a). The schematic of SiOx@C.
(b). TEM image.

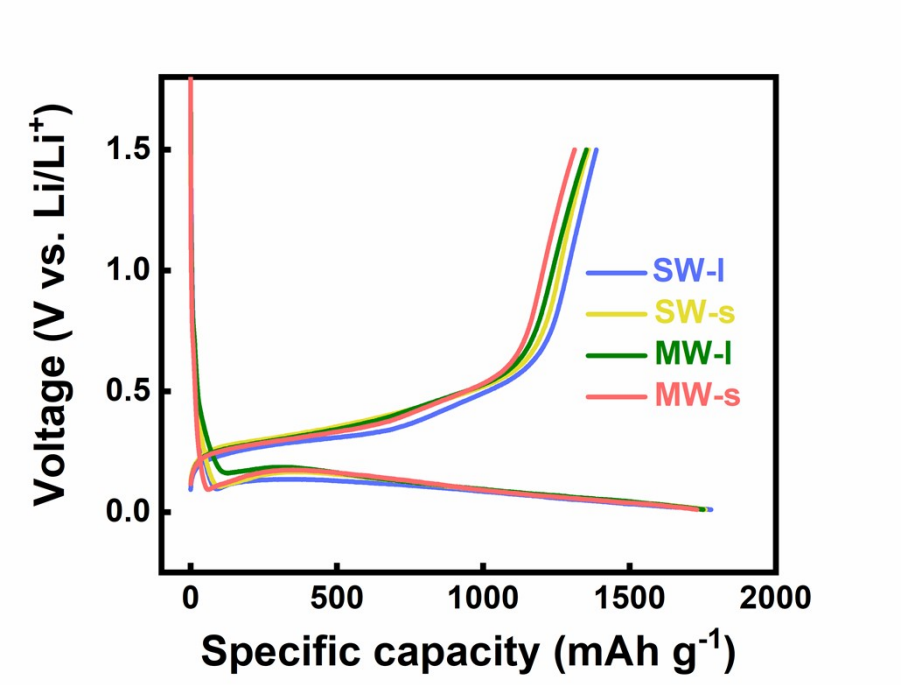

Fig. S4 The corresponding charge and discharge curves of four different electrodes.

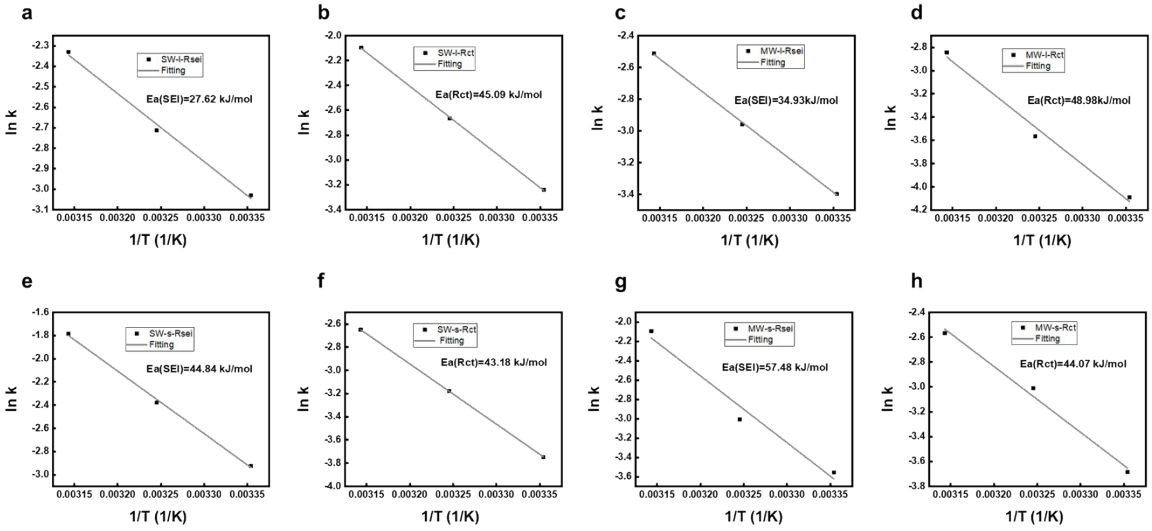

Fig. S5 Fitting results of a-b). the SW-l electrodes. c-d). the MW-l electrodes. e-f). the SW-s electrodes. g-h). the MW-s electrodes.

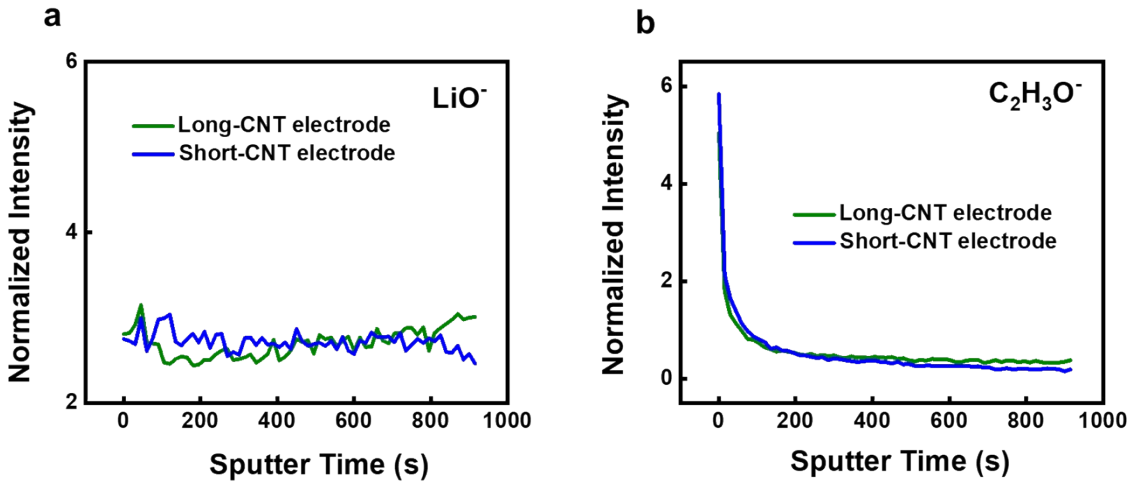

Fig. S6 The normalized intensity changes of selected fragments sputtered from the long-CNT electrodes and short-CNT electrodes.

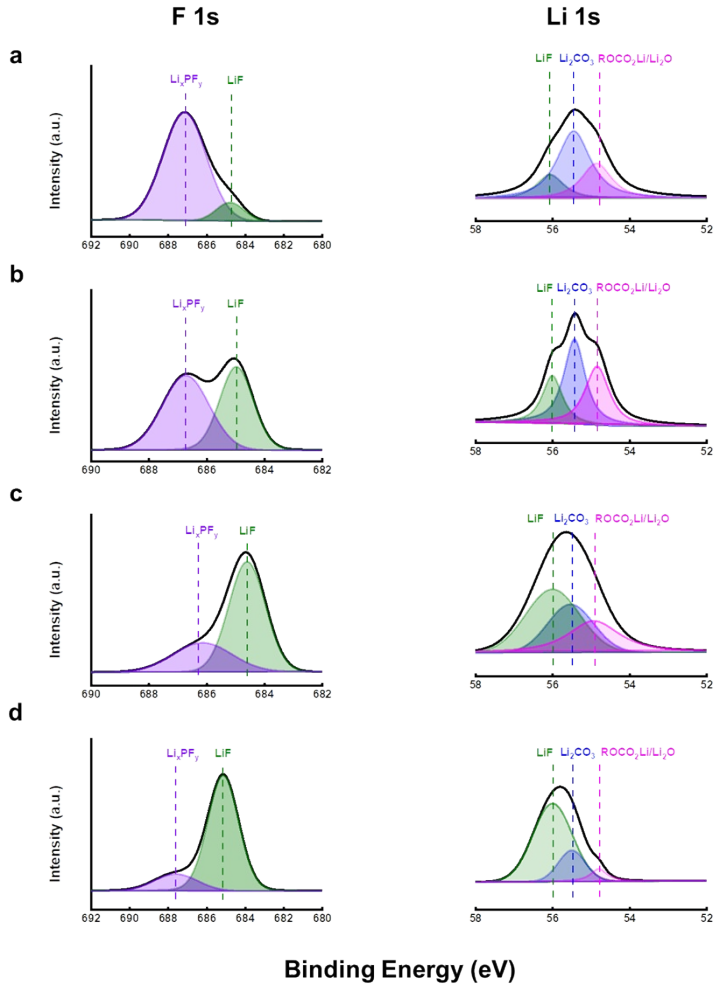

Fig. S7 High-resolution XPS spectra of F 1s and O 1s for (a) the SW-l electrodes. (b) the MW-l electrodes. (c) the SW-s electrodes. (d) the MW-s electrodes.

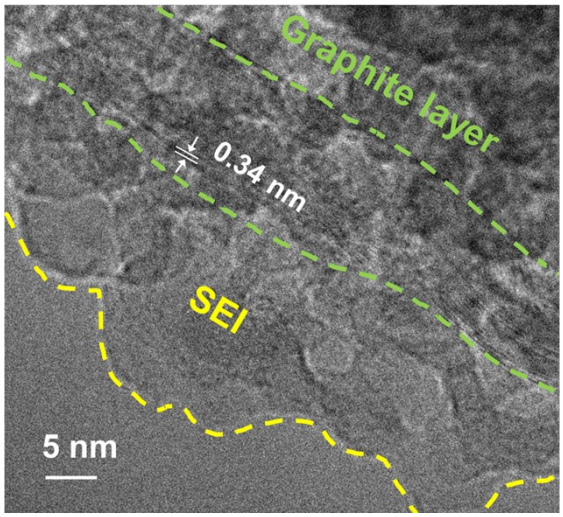

Fig. S8 The Cryo-TEM image of the graphite layer and SEI in long-CNT electrode.

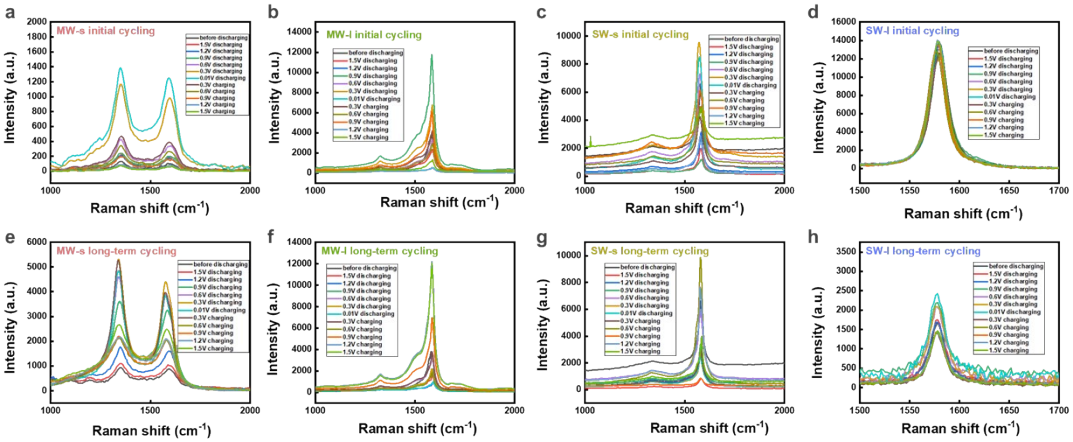

Fig. S9 In-situ Raman results of (a)MW-s, (b)MW-l, (c)SW-s, (d)SW-l during initial cycling and (e)MW-s, (f)MW-l, (g)SW-s, (h)SW-l during long-term cycling.

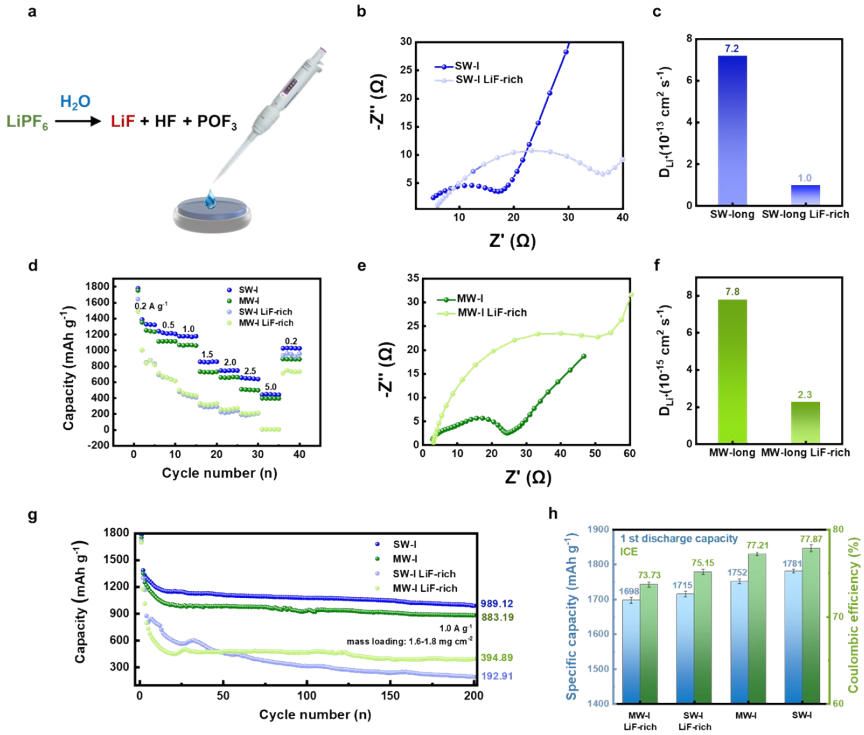

Fig. S10 The performances of LiF-rich electrodes.

(a). The mechanism and illustration of in situ hydrolysis experiments;

(b-c).EIS spectra and D_{Li}^{+} of SW-l and SW-l LiF-rich electrodes;

(d). Rate performances from 0.2 to 5.0 A g^{-1};

(e-f). EIS spectra and D_{Li}^{+} of MW-l and MW-l LiF-rich electrodes;

(g). Long-term cycling performance, for 200 cycles;

(h). ICE and 1st discharge capacity.

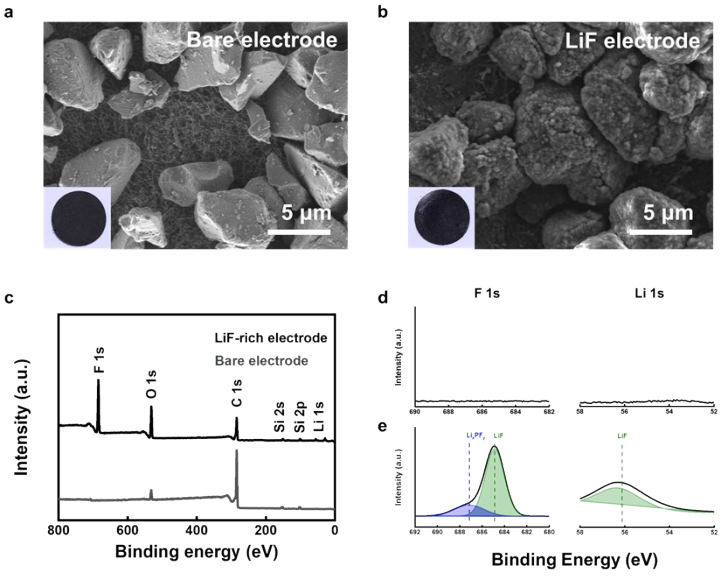

Fig. S11 Morphology and composition of bare and LiF-rich electrodes.

SEM images and inset photos of a) bare electrode and b) LiF-rich electrode. c) The XPS spectra of bare electrode and LiF-rich electrode. F 1s and Li 1s spectra of d) bare electrode, and e) LiF-rich electrode.

Table S1. The length, diameter, aspect ratio and stiffness of different CNTs.

Sample	Length [μm]	Diameter [nm]	Aspect ratio	Stiffness [N/m]
SW-l	1044	2	522000	0.003
MW-l	1022	8	127750	0.054
SW-s	2.5	2	1250	1.382
MW-s	2	8	250	27.646

Table S2. The impedance data and the lithium-ion diffusion coefficient (D_{Li^+}) for the SW-l electrode.

Sample	Re [Ω]	Rsei[Ω]	Rct [Ω]	D_{Li^+} [cm^2/s]
SW-l 25 ℃	1.47	20.17	25.55	7.20×10^{-13}
SW-l 35 ℃	2.14	15.07	14.38	2.85×10^{-12}
SW-l 45 ℃	2.73	10.27	8.14	9.66×10^{-12}

Table S3. The impedance data and the lithium-ion diffusion coefficient (D_{Li^+}) for the MW-l electrode.

Sample	Re [Ω]	Rsei[Ω]	Rct [Ω]	D_{Li^+} [cm^2/s]
MW-l 25 ℃	6.70	29.89	59.64	7.79×10^{-15}
MW-l 35 ℃	3.70	19.29	35.30	3.36×10^{-14}
MW-l 45 ℃	2.21	12.32	17.18	3.23×10^{-13}

Table S4. The impedance data and the lithium-ion diffusion coefficient (D_{Li^+}) for the SW-s electrode.

Sample	Re [Ω]	Rsei[Ω]	Rct [Ω]	D_{Li^+} [cm^2/s]
SW-s 25 ℃	5.40	18.60	42.36	1.79×10^{-13}
SW-s 35 ℃	6.45	10.80	24.02	1.90×10^{-12}
SW-s 45 ℃	5.77	5.96	14.17	4.62×10^{-12}

Table S5. The impedance data and the lithium-ion diffusion coefficient (D_{Li^+}) for the MW-s electrode.

Sample	Re [Ω]	Rsei[Ω]	Rct [Ω]	D_{Li^+} [cm^2/s]
MW-s 25 ℃	4.24	35.03	39.82	2.36×10^{-13}
MW-s 35 ℃	3.46	20.26	20.28	1.00×10^{-12}
MW-s 45 ℃	7.87	8.11	13.05	6.24×10^{-12}

Table S6. The calculated activation energy (E_a) for Li^+ diffusion.

Sample	SEI [kJ/mol]	Charge Transfer [kJ/mol]	D_{Li^+} [kJ/mol]
SW-l|SiO_x@C	27.62	45.09	102.40
MW-l|SiO_x@C	34.93	48.98	146.47
SW-s|SiO_x@C	44.84	43.18	128.61
MW-s|SiO_x@C	57.48	44.07	128.93

Table S7. The ionic migration barrier from references.

Species	Energy barriers of Li^+ diffusion [eV]

LiF	0.729
Li_2CO_3	0.227-0.491
Li_2O	0.152
Li_3N	0.007-0.038

Table S8. The lithium-ion diffusion coefficient of different electrodes.

Sample	D_{Li^+} [cm^2/s]
SW-l|SiO_x@C	7.20×10^{-13}
SW-l|SiO_x@C LiF-rich	1.00×10^{-13}
MW-l|SiO_x@C	7.79×10^{-15}
MW-l|SiO_x@C LiF-rich	2.28×10^{-15}

Table S9. G-band shifts of the CNT under different potentials in electrolyte (current:0.2 mA).

	before discharging	1.5V discharging	1.2V discharging	0.9V discharging	0.6V discharging	0.3V discharging
G band (cm^1)	1588.04	1588.03	1587.87	1588.18	1588.07	1588.17
Shifts (cm^{-1})	0	-0.01	-0.17	0.14	0.03	0.13
	0.01V discharging	0.3V charging	0.6V charging	0.9V charging	1.2V charging	1.5V charging
G band (cm^1)	1588.04	1588.18	1588.06	1588.08	1588.01	1588.08
Shifts (cm^{-1})	0	0.14	0.02	0.04	-0.03	0.04

Table S10. G-band shifts of the CNT under different potentials in electrolyte (current:1 mA).

	before discharging	1.5V discharging	1.2V discharging	0.9V discharging	0.6V discharging	0.3V discharging
G band (cm^1)	1588.03	1588.03	1587.98	1588.12	1588.17	1588.08
Shifts (cm^{-1})	0	0	-0.05	0.09	0.14	0.05
	0.01V discharging	0.3V charging	0.6V charging	0.9V charging	1.2V charging	1.5V charging
G band (cm^1)	1588.09	1588.11	1588.16	1588.10	1588.02	1588.08
Shifts (cm^{-1})	0.06	0.08	0.13	0.07	-0.01	0.05

Table S11. G-band shifts and corresponding stress of CNT in the SW-l electrode under different potentials in initial cycling.

	before discharging	1.5V discharging	1.2V discharging	0.9V discharging	0.6V discharging	0.3V discharging

G band (cm^1)	1581.14	1579.56	1579.68	1580.22	1578.76	1579.62
Shifts (cm^{-1})	0	-1.58	-1.46	-0.92	-2.38	-1.52
Stress (GPa)	0	2.17	2.01	1.27	3.27	2.09
	0.01V discharging	0.3V charging	0.6V charging	0.9V charging	1.2V charging	1.5V charging
G band (cm^1)	1580.03	1580.13	1576.6	1577.75	1578.59	1578.81
Shifts (cm^{-1})	-1.11	-1.01	-4.54	-3.39	-2.55	-2.33
Stress (GPa)	1.53	1.39	6.24	4.66	3.51	3.20

Table S12. G-band shifts and corresponding stress of CNT in the MW-l electrode under different potentials in initial cycling.

	before discharging	1.5V discharging	1.2V discharging	0.9V discharging	0.6V discharging	0.3V discharging
G band (cm^1)	1577.47	1575.62	1575.84	1574.77	1574.80	1574.08
Shifts (cm^{-1})	0	-1.85	-1.63	-2.70	-2.67	-3.39
Stress (GPa)	0	2.54	2.24	3.71	3.67	4.67
	0.01V discharging	0.3V charging	0.6V charging	0.9V charging	1.2V charging	1.5V charging
G band (cm^1)	1573.77	1574.44	1575.11	1575.84	1576.84	1576.94
Shifts (cm^{-1})	-3.70	-3.03	-2.36	-1.63	-0.63	-0.53
Stress (GPa)	5.09	4.17	3.25	2.24	0.87	0.73

Table S13. G-band shifts and corresponding stress of CNT in the SW-s electrode under different potentials in initial cycling.

	before discharging	1.5V discharging	1.2V discharging	0.9V discharging	0.6V discharging	0.3V discharging
G band (cm^1)	1578.60	1578.67	1579.51	1578.05	1576.29	1573.85
Shifts (cm^{-1})	0	0.07	0.91	-0.55	-2.31	-4.75
Stress (GPa)	0	-0.10	-1.25	0.75	3.18	6.53
	0.01V discharging	0.3V charging	0.6V charging	0.9V charging	1.2V charging	1.5V charging
G band (cm^1)	1572.81	1574.00	1575.81	1574.82	1575.20	1578.74
Shifts (cm^{-1})	-5.79	-4.60	-2.79	-3.78	-3.40	0.14
Stress (GPa)	7.96	6.33	3.84	5.20	4.68	-0.19

Table S14. G-band shifts and corresponding stress of CNT in the MW-s electrode under different

potentials in initial cycling.

	before discharging	1.5V discharging	1.2V discharging	0.9V discharging	0.6V discharging	0.3V discharging
G band (cm^1)	1591.62	1591.56	1592.34	1592.45	1590.89	1590.7
Shifts (cm^{-1})	0	-0.06	0.72	0.83	-0.73	-0.92
Stress (GPa)	0	0.08	-0.99	-1.14	1.00	1.27
	0.01V discharging	0.3V charging	0.6V charging	0.9V charging	1.2V charging	1.5V charging
G band (cm^1)	1589.94	1592.72	1589.72	1590.91	1593.12	1589.64
Shifts (cm^{-1})	-1.68	1.1	-1.9	-0.71	1.5	-1.98
Stress (GPa)	2.31	-1.51	2.61	0.98	-2.06	2.72

Table S15. G-band shifts and corresponding stress of CNT in the SW-l electrode under different potentials in long-term cycling.

	before discharging	1.5V discharging	1.2V discharging	0.9V discharging	0.6V discharging	0.3V discharging
G band (cm^1)	1577.82	1577.77	1592.34	1592.45	1590.89	1590.7
Shifts (cm^{-1})	0	-0.05	-0.25	-0.41	-0.37	-0.32
Stress (GPa)	0	0.07	0.34	0.56	0.51	0.44
	0.01V discharging	0.3V charging	0.6V charging	0.9V charging	1.2V charging	1.5V charging
G band (cm^1)	1589.94	1592.72	1589.72	1590.91	1593.12	1589.64
Shifts (cm^{-1})	-0.44	-0.20	-0.15	0	0.16	0.13
Stress (GPa)	0.61	0.21	0.21	0	-0.22	-0.18

Table S16. G-band shifts and corresponding stress of CNT in the MW-l electrode under different potentials in long-term cycling.

	before discharging	1.5V discharging	1.2V discharging	0.9V discharging	0.6V discharging	0.3V discharging
G band (cm^1)	1577.47	1579.62	1579.22	1578.05	1578.76	1577.07
Shifts (cm^{-1})	0	2.15	1.75	0.58	1.29	-0.40
Stress (GPa)	0	-2.96	-2.41	-0.80	-1.77	0.55
	0.01V discharging	0.3V charging	0.6V charging	0.9V charging	1.2V charging	1.5V charging
G band (cm^1)	1576.24	1576.93	1577.37	1578.16	1577.53	1578.31

Shifts (cm^{-1})	-1.23	-0.54	-0.10	0.69	0.06	0.84
Stress (GPa)	1.69	0.74	0.14	-0.95	-0.08	-1.16

Table S17. G-band shifts and corresponding stress of CNT in the SW-s electrode under different potentials in long-term cycling.

	before discharging	1.5V discharging	1.2V discharging	0.9V discharging	0.6V discharging	0.3V discharging
G band (cm^{1})	1578.60	1580.71	1578.33	1578.02	1577.54	1577.33
Shifts (cm^{-1})	0	2.11	-0.27	-0.58	-1.06	-1.27
Stress (GPa)	0	-2.90	0.37	0.80	1.46	1.75
	0.01V discharging	0.3V charging	0.6V charging	0.9V charging	1.2V charging	1.5V charging
G band (cm^{1})	1576.36	1577.17	1577.37	1579.19	1578.65	1581.21
Shifts (cm^{-1})	-2.24	-1.43	-1.23	0.59	0.05	2.61
Stress (GPa)	3.08	1.97	1.69	-0.81	-0.07	-3.59

Table S18. G-band shifts and corresponding stress of CNT in the MW-s electrode under different potentials in long-term cycling.

	before discharging	1.5V discharging	1.2V discharging	0.9V discharging	0.6V discharging	0.3V discharging
G band (cm^{1})	1581.43	1587.88	1585.04	1583.64	1580.92	1580.12
Shifts (cm^{-1})	0	6.45	3.61	2.21	-0.51	-1.31
Stress (GPa)	0	-8.87	-4.96	-3.04	0.70	1.80
	0.01V discharging	0.3V charging	0.6V charging	0.9V charging	1.2V charging	1.5V charging
G band (cm^{1})	1579.67	1579.63	1580.83	1580.52	1580.91	1581.95
Shifts (cm^{-1})	-1.76	-1.8	-0.60	-0.91	-0.52	0.52
Stress (GPa)	2.42	2.48	0.83	1.25	0.72	-0.72